



# A Study of Spectral Variability Between Flaring and Nonflaring State in M74 X-1

Aman Upadhyay<sup>1</sup> , Tanuman Ghosh<sup>2</sup> , and Vikram Rana<sup>1</sup> <sup>1</sup> Astronomy and Astrophysics, Raman Research Institute, C. V. Raman Avenue, Sadashivanagar, Bangalore 560080, India<sup>2</sup> Inter-University Centre for Astronomy and Astrophysics, Ganeshkhind, Pune 411007, India

Received 2024 August 18; revised 2025 June 13; accepted 2025 June 21; published 2025 August 18

## Abstract

We conducted an extensive long-term spectral and timing study of the ultraluminous X-ray (ULX) source M74 X-1, using data taken between 2001 and 2021 by Chandra and XMM-Newton X-ray observatories. Our analysis shows that flares are present in some observations, whereas they are absent in others. The flaring state exhibits two-component spectra at a lower average flux level, whereas the nonflaring state displays single-component spectra at a higher average flux level. The M74 X-1 spectra are best described by the combination of accretion disk and Comptonization components, dual thermal disk blackbody model, and a modified multitemperature disk blackbody model. Using the dual thermal disk blackbody model, we obtain cool and hot temperatures of  $T_{\text{in}}$  (cool) =  $0.38^{+0.08}_{-0.06}$  keV and  $T_{\text{in}}$  (hot) =  $1.67^{+0.18}_{-0.13}$  keV, respectively, suggesting two temperature emitting regions and indicating possible presence of outflowing wind along with the accretion disk. We found a Gaussian feature at  $E_{\text{line}} = 0.96^{+0.05}_{-0.11}$  keV with  $\sigma = 0.11^{+0.13}_{-0.06}$  keV in the spectra of the flaring state, which can be interpreted as the unresolved wind feature in the system when compared to similar feature seen in other ULX sources. Plotting the hardness luminosity diagram, we get a trend of increasing hardness with luminosity, suggesting the presence of geometrical beaming in a low-inclination system. Additionally, using the hot disk blackbody component from the dual thermal disk blackbody model, we estimate the mass of the compact object to be  $M = 7.1^{+1.4}_{-1.3} M_{\odot}$ , classifying it as a stellar-mass black hole and confirming super-Eddington accretion in the system.

*Unified Astronomy Thesaurus concepts:* [Ultraluminous x-ray sources \(2164\)](#); [X-ray astronomy \(1810\)](#); [Accretion \(14\)](#)

## 1. Introduction

Ultraluminous X-ray (ULX) sources are extragalactic non-nuclear accreting binaries with X-ray luminosity exceeding the Eddington luminosity ( $L_X > 10^{39} \text{ erg s}^{-1}$ ) of a stellar-mass black hole ( $\sim 10 M_{\odot}$ ) (P. Kaaret et al. 2017; A. King et al. 2023). Initially, these sources were perceived to be the scaled-up version of galactic black hole binaries (GBHBs) and were considered to be intermediate mass black holes (IMBHs) accreting at the sub-Eddington rates due to their low disk temperature (E. J. Colbert & R. F. Mushotzky 1999; J. M. Miller et al. 2004). However, the high quality XMM-Newton observations have shown that the ULX source spectra are characterized by features such as spectral curvature between 2 and 10 keV along with soft excess below 2 keV (e.g., A.-M. Stobbart et al. 2006), which are distinctive when compared to the GBHBs accreting at sub-Eddington rates. T. P. Roberts (2007) and J. C. Gladstone et al. (2009) proposed that such spectral curvature is a characteristic feature of a new state, the *ultraluminous state*, where the accretion is super-Eddington on a stellar-mass compact object. This was further reaffirmed by the discovery of coherent pulsations in ULX M82 X-2, which proved the existence of a neutron star, and hence the existence of super-Eddington accretion in the system (M. Bachetti et al. 2014). Several ULX pulsars have since been discovered, which show pulsations (F. Fürst et al. 2016; G. L. Israel et al. 2017a, 2017b; S. Carpano et al. 2018; R. Sathyaprakash et al. 2019; G. R. Castillo et al. 2020) along with some ULX sources which have shown pulsations in the

outbursts (S. Tsygankov et al. 2017; C. A. Wilson-Hodge et al. 2018; G. Vasilopoulos et al. 2020). Furthermore, the discovery of a cyclotron resonance scattering feature in M51 X-8 (M. Brightman et al. 2018) revealed that even nonpulsating ULX sources could harbor neutron stars.

The spectra of ULX sources are broadly classified into three categories using a combination of an accretion disk and a power-law model in the 0.3–10.0 keV energy range (A. D. Sutton et al. 2013; P. Kaaret et al. 2017). Typically, broadened disk spectra appear like a single, broad continuum with inner disk temperature  $T_{\text{in}} > 0.5$  keV and ratio of the flux of the power-law component to the flux of the disk component,  $\frac{F_{\text{pl}}}{F_{\text{disk}}}$  (0.3–1.0 keV)  $< 5$ . This spectral category corresponds to the lowest luminosity regime of ULX sources ( $\sim 1\text{--}3 \times 10^{39} \text{ erg s}^{-1}$ ). For  $\frac{F_{\text{pl}}}{F_{\text{disk}}}$  (0.3–1.0 keV)  $> 5$ , with  $T_{\text{in}} > 0.5$  keV, the spectra are classified as an ultraluminous regime with a comparatively higher luminosity than a broadened disk state. For  $T_{\text{in}} < 0.5$  keV, spectra are always in this ultraluminous regime. Depending on the power-law photon index, this ultraluminous state is further classified into two different subcategories, i.e., spectra with  $\Gamma < 2$  are categorized as “hard ultraluminous,” whereas  $\Gamma > 2$  are classified as “soft ultraluminous” states. If the spectra are dominated by a single blackbody component with  $kT \lesssim 0.1$  keV and with the bolometric luminosity of  $\sim 10^{39} \text{ erg s}^{-1}$ , then the source is defined as an ultraluminous supersoft source (A. Kong & R. Di Stefano 2003; H. Feng et al. 2016; C. Pinto et al. 2017).

Broadband spectral analysis of ULX sources has shown that their spectra in the 0.3–20 keV X-ray band can be characterized by two thermal disk components, while an additional component, such as coronal Comptonization or emission from the accretion column, is required to explain the high-energy band for nonmagnetic and magnetic accretors, respectively



Original content from this work may be used under the terms of the [Creative Commons Attribution 4.0 licence](#). Any further distribution of this work must maintain attribution to the author(s) and the title of the work, journal citation and DOI.

**Table 1**  
List of Observations Studied in this Work Taken by Chandra and XMM-Newton between 2001 and 2021

Obs. ID	Mission	Detector	Flaring/Nonflaring	Date	Ontime (ks)
2057	CHANDRA	ACIS-S	Flaring	19-06-2001	45.4
2058	CHANDRA	ACIS-S	Flaring	19-10-2001	46.1
0154350101	XMM-Newton	MOS1, MOS2, pn	Flaring	02-02-2002	28, 27, 22
14801	CHANDRA	ACIS-S	Nonflaring	21-08-2013	9.8
16000	CHANDRA	ACIS-S	Nonflaring	21-09-2013	39.6
16001	CHANDRA	ACIS-S	Nonflaring	07-10-2013	14.7
16484	CHANDRA	ACIS-S	Nonflaring	10-10-2013	14.7
16485	CHANDRA	ACIS-S	Nonflaring	11-10-2013	8.9
16002	CHANDRA	ACIS-S	Nonflaring	14-11-2013	37.6
16003	CHANDRA	ACIS-S	Nonflaring	15-12-2013	40.4
0864270101	XMM-Newton	MOS1, MOS2, pn	Nonflaring	13-01-2021	38, 39, 26

(D. Walton et al. 2018, 2020). The cool disk in the dual thermal disk model refers to the emission from the outer disk or the reprocessed soft photons coming from the optically thick outflows produced due to super-Eddington accretion in the system (J. Poutanen et al. 2007; J. J. E. Kajava & J. Poutanen 2009), while the hot component comes from the inner regions of the accretion disk or corona (D. J. Walton et al. 2014; D. Walton et al. 2015; W. Luangtip et al. 2016).

A large number of ULX sources have been observed to date (D. J. Walton et al. 2022), with some exhibiting persistent behavior while others show extreme variability in which the flux can change over an order of magnitude. These variable sources have shown short-term timing variability in terms of periodic oscillation and quasi-periodic oscillation (QPO). Some of the sources, such as NGC 7456 ULX-1 (F. Pintore et al. 2020), NGC 6946 ULX-4 (H. P. Earnshaw et al. 2019), NGC 4559 X-7 (F. Pintore et al. 2021), NGC 1313 X-1 (D. Walton et al. 2020), M51 ULX-7 (H. M. Earnshaw et al. 2016), NGC 4395 ULX-1 (T. Ghosh et al. 2022), and NGC 3621 ULX-1 (S. Motta et al. 2020), have shown flaring events in the X-ray light curve that have helped in learning about the accretion processes in these sources.

M74 (NGC 628) is a nearby spiral galaxy located at a distance of 9.7 Mpc (S. Avdan et al. 2023). It hosts two ULX sources, M74 X-1 and M74 X-2, which are 1.5° apart. Out of these, M74 X-2 is a transient source that was above the detection limit in only one XMM-Newton observation (Obs. ID: 0154350101) in February 2002 (R. Soria & A. K. Kong 2002). M74 X-1 has been studied earlier, and flaring activity was reported in the source with its luminosity varying in the range of  $\sim 5 \times 10^{38} \text{ erg s}^{-1}$  to  $\sim 1.2 \times 10^{40} \text{ erg s}^{-1}$  in a time period of half an hour (M. Krauss et al. 2005).

In this paper, we have performed an extensive long-term spectral and timing study of M74 X-1, using data from several observations taken between 2001 and 2021 by Chandra and XMM-Newton, listed in Table 1. Previously, M. Krauss et al. (2005) and J.-F. Liu et al. (2005) studied 2001 Chandra and XMM observations and detected flaring events. Here, we study all available observations from 2001 to 2021. The data reduction procedures are described in Section 2. Results from spectral and timing analysis are reported in Section 3. We discuss the physical implications of our analysis in Section 4 and conclude our findings in Section 5.

## 2. Observation and Data Reduction

M74 was observed 16 times between 2001 and 2021 by XMM-Newton and Chandra. Of 16 observations, M74 X-1 was visible in 11 observations. In the remaining five observations, it was intrinsically faint, or the statistics were poor for any meaningful scientific analysis due to the low exposure time of the observations. We analyze all 11 observations (listed in Table 1), including the three previously studied observations in which flaring was reported (obs ID: 2057, 2058, 0154350101) by M. Krauss et al. (2005) and J.-F. Liu et al. (2005), and compare the spectral and timing properties between the flaring and nonflaring states.

### 2.1. XMM-Newton

The XMM-Newton data were extracted by using standard SAS software v21.0.0. The EPIC MOS and pn data were extracted using `emproc` and `epproc`. Significantly high background epochs were observed in both 2002 (Obs ID: 0154350101) and 2021 (Obs ID: 0864270101) observations, which were removed by creating good time intervals (GTIs) using the task `tabgtigen`. The durations of the GTIs are 28, 27, 22 ks and 38, 39, and 26 ks for MOS1, MOS2, and pn for the 2002 and 2021 observations, respectively. These GTI files are used to create clean event files, which are further used to extract spectra and light curves using `evselect`. We apply the standard filter, i.e., `PATTERN ≤ 4` for pn, and `PATTERN ≤ 12` for MOS1 and MOS2. Barycentric correction of the events was done using the tool `barycen`. We use a 20'' radius circle centered at R.A., decl. = 138:40:33.74, −45:42:56.75 (M. Krauss et al. 2005) to extract source photons for both observations. We use a 40'' radius region without source contamination from the same CCD to extract background photons for both observations (shown in Figure 1). The spectra were binned using `specgroup` with a minimum of 20 counts per bin to allow for fits with  $\chi^2$  statistics and an oversample of 3 to ensure that each group is at least 1/3 of full width at half-maximum resolution wide. Corresponding RMFs and ARFs were created using `rmfgen` and `arfgen`, respectively.

### 2.2. Chandra

We analyze Chandra ACIS-S data using Chandra Interactive Analysis of Observations (CIAO) v4.15 software, along with

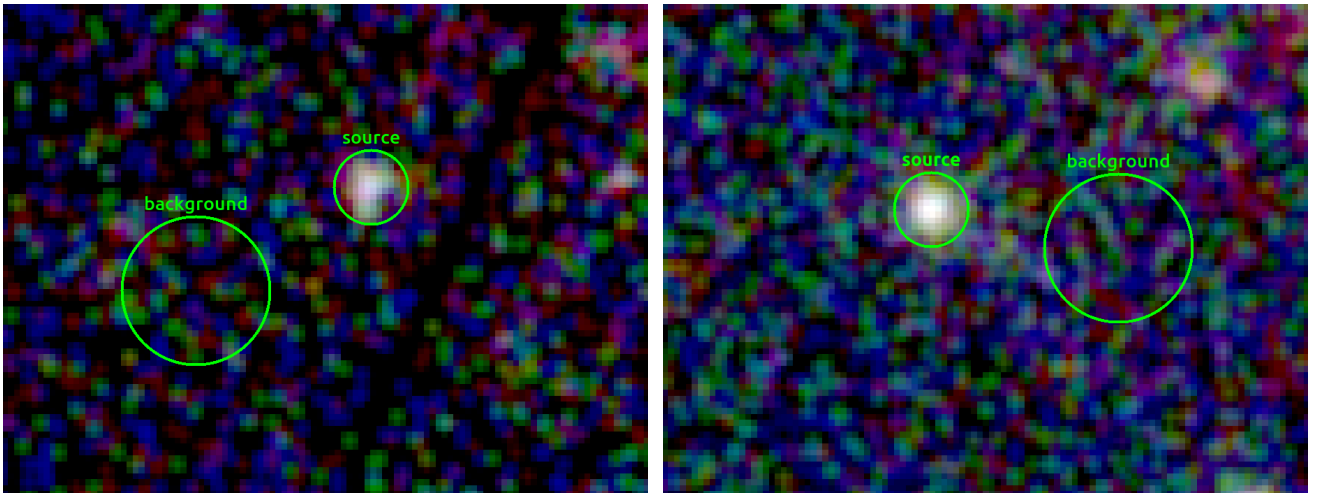


**Figure 1.** Source and background region selection for Obs. ID 0154350101 (left) and 0864270101 (right) for the MOS1 detector. The figure is plotted in a red, green and blue frame where red corresponds to the events in (0.2–1.5 keV), green corresponds to events in (1.5–2.5 keV), and blue corresponds to events in (2.5–10 keV).

the calibration files CALDB v4.10.4. The level 2 event files are obtained with `chandra_repro` in CIAO. `Wavdetect` is used to identify the source pixels in the image, which is further used to create a background file by excluding these pixels from the image. All observations are searched for the time intervals of high background flaring, and little to no background flaring was seen in all Chandra observations, which is also removed using the command `deflare`. To verify that the pileup does not affect the spectrum, we use the pileup algorithm implemented in PIMMS, where we find that the pileup fraction in all the observations is  $<5\%$ . For source and background region selection, we use elliptical and circular regions for different observations according to the spread of the photons on the detector. Elliptical areas were selected for Obs. IDs: 2057, 2058, and 16003, whereas for the rest of the Chandra observations, circular source regions of radius  $1''.5$  are selected, which covers the full point-spread function of the sources, and a  $3''.0$  region on the same CCD is selected as a background region. Furthermore, `dmextract` and `specextract` are used to extract light curves and spectra of all the observations.

### 3. Analysis and Results

#### 3.1. Timing Analysis

Previous studies, such as M. Krauss et al. (2005), have reported that M74 X-1 is a highly variable source as seen across observations (Obs. IDs—2057, 2058, 0154350101; M. Krauss et al. 2005) with the count rate changing by an order of magnitude, as illustrated in Figure 2(a). We verify the flaring activity in these observations and find that the rest of the observations have a stable light curve with no flaring activity, as, e.g., shown in Figure 2(b). These flaring events are present in both hard and soft X-ray bands, which we verified by plotting light curves in the soft (0.3–1.0 keV) and hard (1.0–10.0 keV) X-ray energy bands (see Figure 9 in M. Krauss et al. 2005). Earlier studies (M. Krauss et al. 2005; J.-F. Liu et al. 2005) have also suggested the existence of shallow frequency 2 hr QPOs in the power density spectrum of the observations with flaring state. Recently, H. Avdan & S. Avdan (2024) has claimed a similar QPO feature in two more observations (Obs. IDs: 16485 and 16002) in a

nonflaring state. However, the significance of these QPOs is considerably lower compared to the flaring state (H. Avdan & S. Avdan 2024). To search for pulsation in the data, we employ an accelerated search technique with HENACCEL-SEARCH (a task in package HENDRICS v8.0.3; M. Bache-tti 2018). We use this technique for both Chandra and XMM-Newton (EPIC-pn) observations in the energy range (0.3–10.0 keV), in the frequency range (0.01–6.8 Hz) and (0.01–0.15 Hz), for XMM-Newton and Chandra, respectively, to avoid artifacts due to the Nyquist limit. We do not see any sign of pulsations in these observations.

#### 3.2. Spectral Analysis

We use Xspec v12.13.0 (K. Arnaud 1996) to perform the detailed spectral analysis of the ULX M74 X-1. To model the absorption effects caused by neutral absorbers, we have used `tbabs` with updated solar abundances (J. Wilms et al. 2000), with photoionization cross section given by D. Verner et al. (1996). We have used the  $\chi^2$  minimization method for model spectral fitting and report the errors with a 90% confidence range, unless stated otherwise.

We begin the data analysis by plotting the unfolded spectra of all the observations listed in Table 1 to look for any spectral variability by visual inspection. The unfolded spectra are produced using a powerlaw model with zero photon index, essentially a constant model. We plot the unfolded spectra of observations in flaring and nonflaring states separately to see any change in their spectral shape (Figure 3). All observations in the flaring state seem to have a similar spectral shape, with different flux values (Figure 3(a)). Here, variability is seen in both soft (0.3–1.0 keV) and hard (1.0–10.0 keV) energy bands. On the other hand, the nonflaring states have curved spectra that seem to overlap below 1 keV and variable above 1 keV (Figure 3(b)). Out of the eight observations in the nonflaring state, the first six observations (Obs. IDs—14801, 16000, 16001, 16484, 16485, and 16002) show overlapping spectra in the hard X-ray band ( $>1.0$  keV). The remaining two observations (Obs. IDs: 16003 and 0864270101) also have overlapping spectra in the hard X-ray band ( $>1.0$  keV), but the hard X-ray flux of the last two observations ( $(1.52\text{--}2.03) \times 10^{-13} \text{ erg cm}^{-2} \text{ s}^{-1}$ ) is less than the first six observations ( $(2.89\text{--}3.51) \times 10^{-13} \text{ erg cm}^{-2} \text{ s}^{-1}$ ). We begin the spectral analysis with the basic absorbed powerlaw

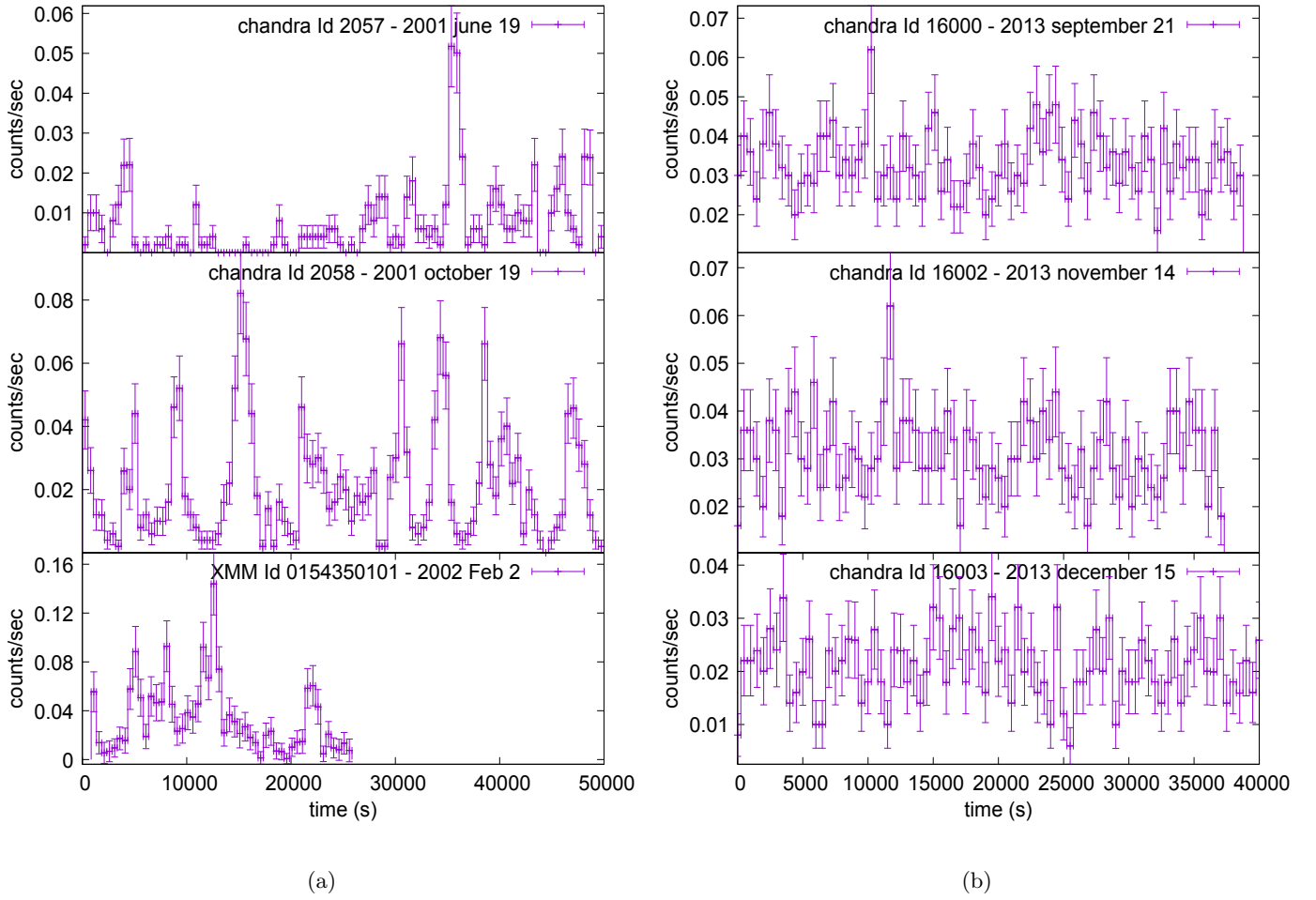


**Figure 2.** Light curves of observations with flaring states (a) and nonflaring states (b), both binned with  $t = 500$  s. For the nonflaring state, light curves of observations (Obs. Ids: 16000, 16002, and 16003) with the highest exposure time have been plotted.

model to see the variation of  $nH$ . While there are fluctuations in the  $nH$  values across different epochs, the values overlap within the error bars. Moreover, because of the spectral difference between flaring and nonflaring states, we analyze them into separate groups. For the observations in the flaring state, linking  $nH$  provides statistically similar results ( $\chi^2/\text{dof} = 84/74$  to  $\chi^2/\text{dof} = 86/76$ ). Here,  $nH$  is not constrained  $< 0.05$ , so we further freeze  $nH$  to the galactic value of 0.048 ( $10^{22}$  atoms  $\text{cm}^{-2}$ ), which gives  $\chi^2/\text{dof} = 88/77$ . This provides an acceptably good fit with excess around 1 keV and some marginal excess at hard energies (above 3 keV) in the residuals, as can be seen in Figure 4(a). We add the `diskbb` component in addition to the power law to see if it provides a better fit. It improves the fit with  $\chi^2/\text{dof} = 71/71$ . The `diskbb` component takes care of the low-energy part in the spectra, whereas the power law is responsible for explaining the hard X-ray part. We see that the inner disk temperature  $T_{\text{in}}$  and  $\Gamma$  values for each spectrum are within error bars, so we further link the  $T_{\text{in}}$  and  $\Gamma$  values between these observations, which gives  $\chi^2/\text{dof} = 73/75$ . (Table 2). Similar inner disk temperature  $T_{\text{in}}$  and  $\Gamma$  values between the observations in the flaring state indicate that the spectra of the flaring state have identical shapes with varying soft and hard X-ray component flux. Due to the spectral similarity among the observations in the flaring state, we group all the observations in the flaring state in Group A. We also observe

excess residue around 1 keV in the spectra of the flaring state, which was not reported in the previous studies. Such a feature has been observed in several other ULX sources, which is believed to arise due to the blend of atomic absorption and emission lines formed by the interaction of hard photons with the wind. These signatures of wind indicate the presence of super-Eddington accretion in the system. We add a Gaussian component to model this 1 keV feature, where we link the Gaussian line energy  $E_l$  and line width  $\sigma$  between the observations. This gives  $E_{\text{line}} = 0.96^{+0.05}_{-0.11}$  keV with  $\sigma = 0.11^{+0.13}_{-0.06}$  keV. Adding Gaussian in `diskbb+powerlaw` model improves the statistics with  $\chi^2/\text{dof} = 55/68$ . There is a degeneracy between the Gaussian and `diskbb` components in the low-energy part, hence the addition of the Gaussian component lowers the inner disk temperature to  $T_{\text{in}} = 0.15^{+0.12}_{-0.07}$  keV but has overlapping values within error bars with the disk temperature when the Gaussian component is not included ( $T_{\text{in}} = 0.28^{+0.04}_{-0.04}$  keV).

For observations in the nonflaring state, linking the  $nH$  for the `powerlaw` model changes the statistics from  $\chi^2/\text{dof} = 322/301$  to  $\chi^2/\text{dof} = 333/308$ , which is statistically similar. Therefore,  $nH$  is linked for further analysis. The power-law model provides a sufficiently good fit to the data, with no requirement of additional `diskbb` component, unlike observations in the flaring state. There is no hard excess or



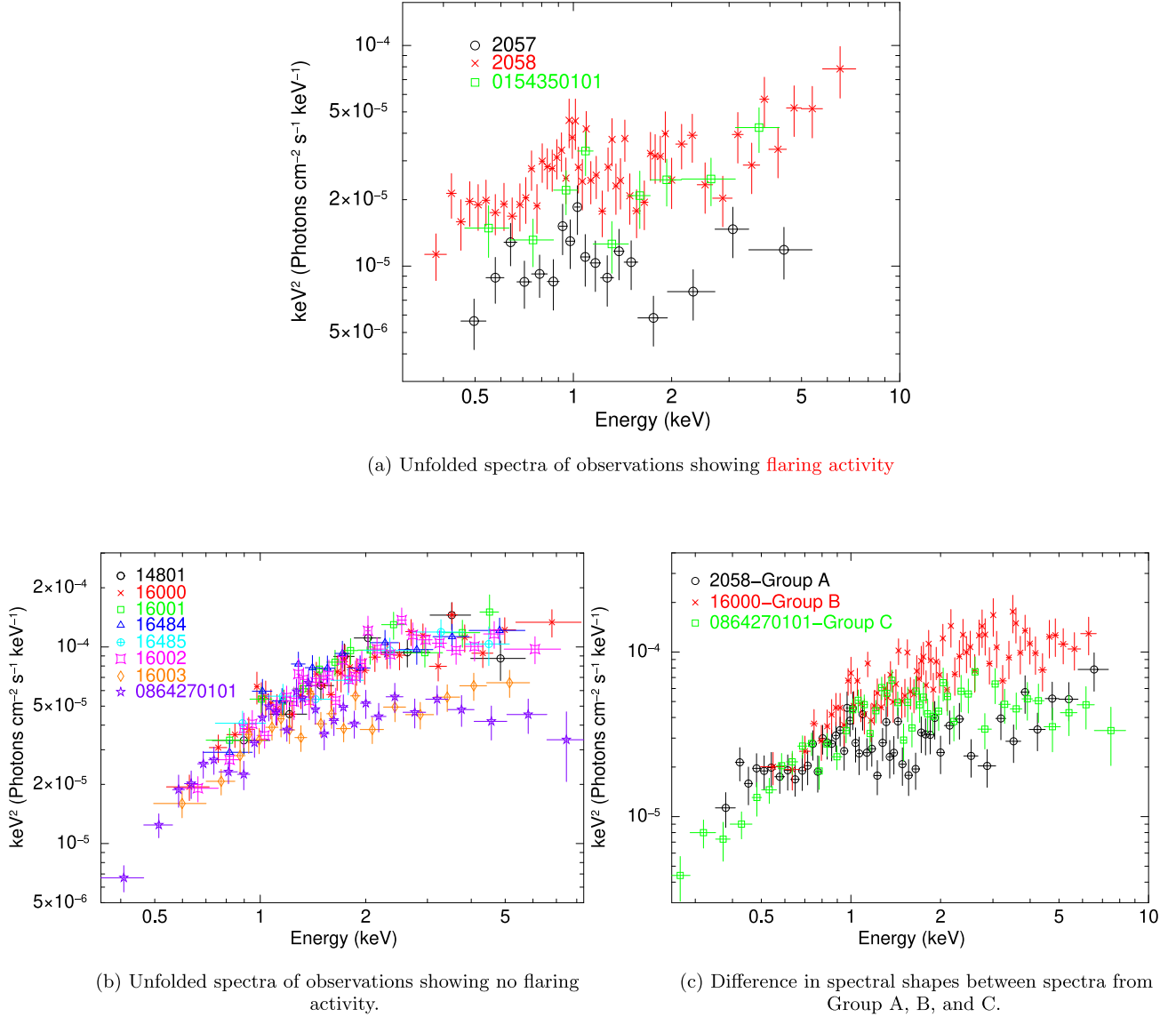


**Figure 3.** Unfolded spectra of observations with flaring state (a) and observations with nonflaring state (b), using the powerlaw model with zero photon index (constant model). Figure (a): All observations with flaring state have similar power law-like spectral shapes with different flux values. Figure (b): Spectra of observations with a nonflaring state seem to overlap below 1 keV and are variable above 1 keV. Figure (c): Different spectral shapes of the spectra from Groups A, B, and C.

residue around 1 keV in the spectra of the nonflaring state (Figure 4(b)).  $\Gamma$  of the first six observations are consistent ( $\Gamma \sim 1.6$ ) within the error bars, except for the last two observations (Obs. IDs: 16003 and 0864270101; Figure 4(c)). The last two observations are relatively softer and have flux values lower than the first six observations. The first six observations of the nonflaring group, which have similar parameter values, are further grouped into Group B. The last two observations, which also have similar parameter values, are grouped into Group C. Group B contains Obs. IDs—14801, 16000, 16001, 16484, 16485, and 16002, and Group C contains Obs. IDs 16003 and 0864270101. To see the spectral difference between the groups, we plot one representative spectrum from each group (Figure 3(c)). Here, we can see different spectral shapes corresponding to the three groups. To check for the presence of any spectral cutoff, a characteristic feature found in ULX sources, we also employed the cutoff

power-law model (`cutoffpl`) to fit the spectra. For observations in a nonflaring state, we link the  $nH$  values between the observations and separately link the e-folding energy  $E_{\text{fold}}$  in Group B and Group C. This gives a sufficiently good fit with  $\chi^2/\text{dof} = 318/306$ , significantly improving the power-law model with  $\Delta\chi^2 = 15$  for 2 degrees of freedom (dof). We see that gamma values are within error bars for Group B and Group C separately, which we linked in the further analysis. We get e-folding energy of  $E_{\text{fold}} = 3.9^{+2.4}_{-1.1}$  keV and  $E_{\text{fold}} > 4.1$  keV for Group B and Group C, respectively. Since the e-folding energies for both groups overlap, we link them, resulting in  $E_{\text{fold}} = 4.6^{+3.4}_{-1.4}$  keV (Table 3), with  $\chi^2/\text{dof} = 327/313$ . Fitting the spectra of the flaring state with the `cutoffpl` model results in an unconstrained e-folding energy. This is also evident in the spectral shape of the observations in the flaring state, which increases sharply after  $\sim 3$  keV. We further freeze the e-folding

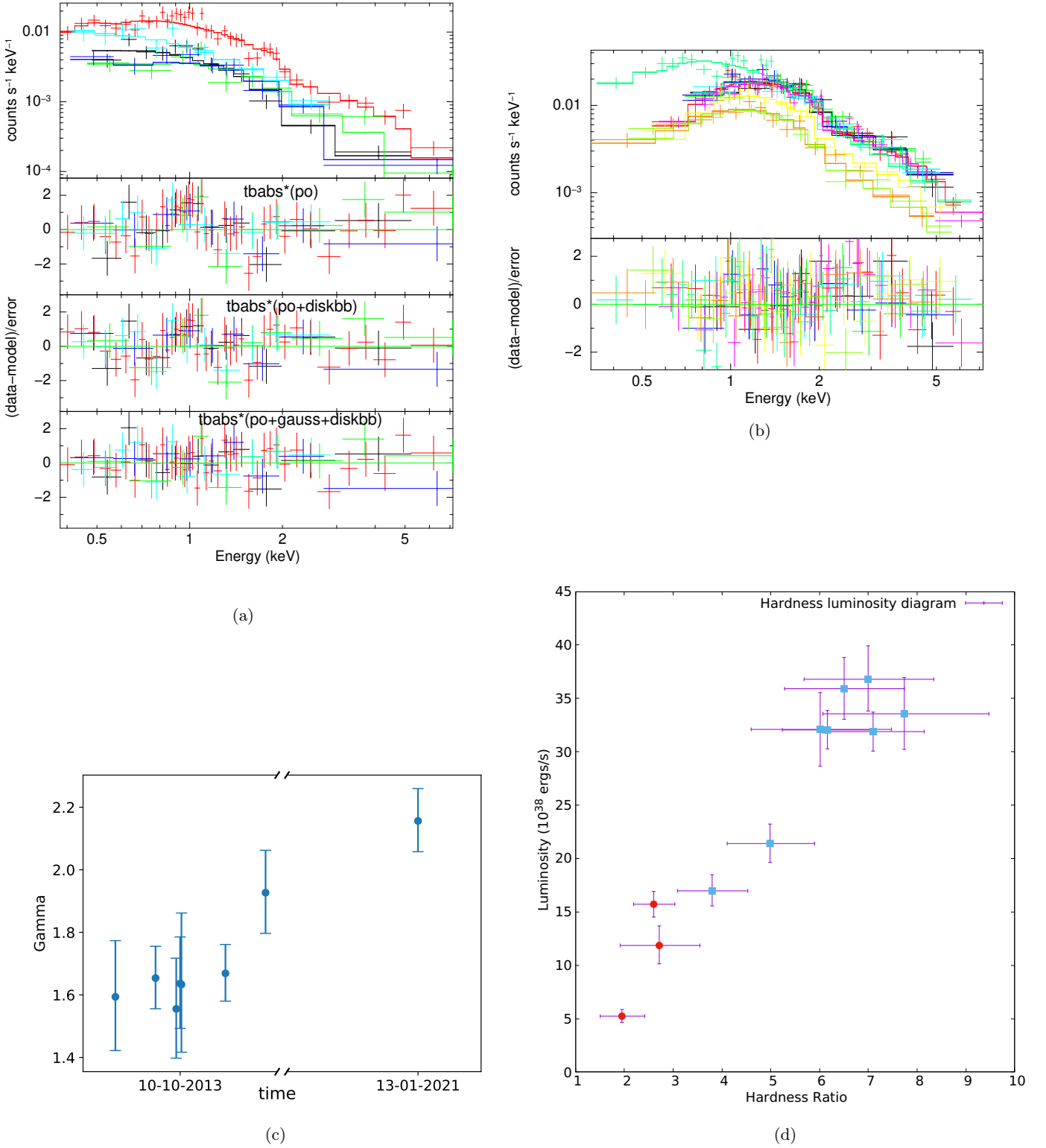


**Figure 4.** (a): Spectra and residuals from the simultaneous fitting of observations in flaring state (Obs. IDs: 2057, 2058, 0154350101) with model  $\text{tbabs}^*(\text{po})$ ,  $\text{tbabs}^*(\text{diskbb}+\text{po})$ , and  $\text{tbabs}^*(\text{diskbb}+\text{gauss}+\text{po})$  for linked  $n\text{H}$ ,  $T_{\text{in}}$ ,  $\Gamma$  and Gaussian parameters. (b): Spectra and residue of observations in nonflaring state with model  $\text{tbabs}^*(\text{po})$  with linked  $n\text{H}$ . (c):  $\Gamma$  evolution of observations with nonflaring state using  $\text{tbabs}^*(\text{po})$  and linked  $n\text{H}$ . (d) Hardness–luminosity diagram for all observations, where hardness is defined as the flux ratio between (1.0–10.0 keV) and (0.3–1.0 keV), while luminosity is calculated for the (0.3–10 keV) energy range. Here, red circles represent observations in the flaring state, and blue squares represent observations in the nonflaring state.

energy to  $E_{\text{fold}} = 4.6$  keV for the flaring state, which we obtain from the fitting of observations with the nonflaring state, to see how the statistics change. This gives a poor fit with  $\chi^2/\text{dof} = 109/77$  and excess in the residuals.

### 3.2.1. $\text{diskbb}+\text{comptt}$

The  $\text{diskbb}+\text{powerlaw}$  provides a good fit for the flaring state. However, in this section, we discuss the use of a more physically motivated model,  $\text{diskbb}+\text{comptt}$ , where

**Table 2**  
Spectral Fitting Results of Observations in Flaring State (Group A)

Obs ID	$nH$ $10^{22}(\text{cm}^{-2})$	Power Law		Disk Blackbody		Gaussian			$\chi^2/\text{dof}$
		$\Gamma$	Norm ( $10^{-5}$ )	$T_{\text{in}}(\text{keV})$	Norm	$E_l(\text{keV})$	$\sigma(\text{keV})$	Norm ( $10^{-5}$ )	
2057	0.048 (a)	$2.12^{+0.20}_{-0.19}$	$1.01^{+0.10}_{-0.11}$	...	...	...	...	...	15/11
	...	$1.29^{+0.30}_{-0.35}$ (b)	$0.41^{+0.21}_{-0.17}$	$0.28^{+0.04}_{-0.04}$ (d)	$0.19^{+0.18}_{-0.08}$	...	...	...	10/9
	...	$1.54^{+0.17}_{-0.26}$ (c)	$0.62^{+0.16}_{-0.13}$	$0.15^{+0.12}_{-0.07}$ (e)	$>0.13$	$0.96^{+0.05}_{-0.11}$ (f)	$0.11^{+0.13}_{-0.06}$ (g)	$0.25^{+0.17}_{-0.17}$	10/6
2058	...	$1.88^{+0.10}_{-0.10}$	$2.76^{+0.16}_{-0.16}$	...	...	...	...	...	44/39
	...	$1.29^{+0.30}_{-0.35}$ (b)	$1.44^{+0.61}_{-0.54}$	$0.28^{+0.04}_{-0.04}$ (d)	$0.40^{+0.31}_{-0.17}$	...	...	...	36/39
	...	$1.54^{+0.17}_{-0.26}$ (c)	$2.00^{+0.35}_{-0.54}$	$0.15^{+0.12}_{-0.07}$ (e)	$>0.20$	$0.96^{+0.05}_{-0.11}$ (f)	$0.11^{+0.13}_{-0.06}$ (g)	$0.45^{+0.28}_{-0.27}$	26/38
01545350101	...	$1.88^{+0.15}_{-0.15}$	$2.06^{+0.29}_{-0.29}$	...	...	...	...	...	29/27
	...	$1.29^{+0.30}_{-0.35}$ (b)	$1.11^{+0.51}_{-0.43}$	$0.28^{+0.04}_{-0.04}$ (d)	$0.28^{+0.25}_{-0.13}$	...	...	...	27/27
	...	$1.54^{+0.17}_{-0.26}$ (c)	$1.55^{+0.34}_{-0.43}$	$0.15^{+0.12}_{-0.07}$ (e)	$>0.10$	$0.96^{+0.05}_{-0.11}$ (f)	$0.11^{+0.13}_{-0.06}$ (g)	$0.30^{+0.25}_{-0.23}$	20/26

**Note.** (a) :  $nH$  fixed to the galactic value. (b) and (c) : Linked  $\Gamma$  between all observations for model  $\text{tbabs}^*(\text{diskbb}+\text{po})$  and  $\text{tbabs}^*(\text{diskbb}+\text{po}+\text{gauss})$ . (d) and (e): Linked  $T_{\text{in}}$  between all observations for model  $\text{tbabs}^*(\text{diskbb}+\text{po})$  and  $\text{tbabs}^*(\text{diskbb}+\text{po}+\text{gauss})$ . (f) and (g): Linked line energy  $E_l$  and line width  $\sigma$ , respectively, between all observations for  $\text{tbabs}^*(\text{diskbb}+\text{gauss}+\text{po})$ .

**Table 3**  
Spectral Fitting Results of Observations in Nonflaring State (Group B + Group C) With Cutoff Power-law Model With Linked  $nH$  and  $E_{\text{fold}}$  and  $\Gamma$

Obs ID	$nH$ $10^{22}(\text{cm}^{-2})$	Cutoff Power Law			$\chi^2/\text{dof}$
		$\Gamma$	$E_{\text{fold}}(\text{keV})$	Norm ( $10^{-5}$ )	
14801	$0.14^{+0.05}_{-0.04}$ (a)	$1.02^{+0.27}_{-0.27}$ (b)	$4.63^{+3.5}_{-1.4}$ (d)	$6.77^{+0.77}_{-0.73}$	15/11
16000	...	...	...	$6.70^{+0.50}_{-0.47}$	61/57
16001	...	...	...	$7.56^{+0.72}_{-0.68}$	17/22
16484	...	...	...	$7.43^{+0.71}_{-0.67}$	20/23
16485	...	...	...	$6.68^{+0.79}_{-0.75}$	13/12
16002	...	...	...	$6.50^{+0.51}_{-0.48}$	57/50
16003	...	$1.52^{+0.28}_{-0.28}$ (c)	...	$5.30^{+0.48}_{-0.44}$	38/36
0864270101	...	...	...	$5.30^{+0.56}_{-0.52}$	106/103

**Note.** Simultaneous fitting with  $\text{tbabs}^*(\text{cutoffpl})$  gives  $\chi^2/\text{dof} = 327/313$ . (a) and (d) :  $nH$  and  $E_{\text{fold}}$  values linked between all observations. (b) and (c): Linked  $\Gamma$  values in Group B and Group C, respectively.

powerlaw in the previous model is replaced by `comptt`. Although `diskbb` is not statistically required in the nonflaring state, we employ this model for both flaring and nonflaring states to compare the relative contributions of the soft and hard components in both these states.

The `comptt` component considers the Comptonization of soft photons by the optically thick corona, where the soft photons are provided by the accretion disk. This interpretation is generally used in the case of sub-Eddington accretion in GBHBs. An alternate interpretation of this model has been proposed where the soft photons are attributed to the massive optically thick outflowing wind instead of the accretion disk, with the hard photons coming from the inner regions of the disk or corona (J. J. E. Kajava & J. Poutanen 2009). This wind could launch from the inner regions of the disk if the accretion flow is super-Eddington. The detection of a 1 keV Gaussian feature in the flaring state of M74 X-1 could indicate a super-Eddington accretion flow with an outflowing wind in the system. Therefore, we adopt the second interpretation of `comptt` in our work.

In the `diskbb+comptt` model, we initially allow the input photon temperature  $T_0$  to vary independently for Groups A, B, and C. Since Groups B and C show similar  $T_0$  values, we link them for further analysis. Similarly, we initially allow the inner disk temperature  $T_{\text{in}}$  to vary independently for these groups. However, because Groups B and C have overlapping

spectra below 1 keV, we link  $T_{\text{in}}$  of the soft component `diskbb` between them. The plasma temperature we obtain is not well constrained, with the best-fit value around  $\sim 2.0$  keV. Therefore, we freeze it at  $T_e \sim 2.0$  keV, which is consistent with the values generally observed in ULX sources (F. Pintore et al. 2014). Furthermore, we set the input photon temperature equal to the inner disk temperature,  $T_0 = T_{\text{in}}$ . This provides us with a good fit with  $\chi^2/\text{dof} = 383/373$ . For Group A, the temperature comes out to be  $T_0 = T_{\text{in}} = 0.26^{+0.06}_{-0.06}$  keV, whereas for Groups B and C,  $T_0 = T_{\text{in}} = 0.61^{+0.15}_{-0.18}$  keV (Table 4). We get very high optical depth  $\tau \sim 8.0$  for plasma temperature of  $T_e = 2.0$  keV for both flaring and nonflaring states. This state is different from the state we generally find in GBHBs, where we get hot and optically thin corona  $\tau \sim 1$  (J. C. Gladstone et al. 2009; F. Pintore et al. 2014). We see that the optical depth is consistent within error bars for both flaring and nonflaring states. We confirmed this by linking the optical depth of all observations, which changes the statistics from  $\chi^2/\text{dof} = 383/373$  to  $\chi^2/\text{dof} = 401/383$ , practically providing the same fit statistics. This gives us a common optical depth of  $\tau = 8.6^{+0.76}_{-0.53}$ .

We plot the hardness–luminosity diagram (Figure 4(d)) for both flaring (red circle) and nonflaring states (blue square). Here, hardness is defined as the flux ratio between (1.0–10.0 keV) and (0.3–1.0 keV), which is calculated using `cflux` convolution model. The luminosity is unabsorbed,

**Table 4**  
Spectral Fitting Results of all Observations Using Model `tbabs*(diskbb+comptt)`

Obs Ids	$nH$ ( $10^{22} \text{ cm}^{-2}$ )	$T_0 = T_{\text{in}}$ (keV)	$\tau$	Norm(comptt) ( $10^{-5}$ )	Norm(diskbb)	flux ( $10^{-13} \text{ erg cm}^{-2} \text{ s}^{-1}$ )	$\chi^2/\text{dof}$
2057	0.048 (a)	$0.26^{+0.06}_{-0.06}$ (b)	$9.49^{+9.8}_{-3.4}$	$0.55^{+0.39}_{-0.22}$	$0.29^{+0.94}_{-0.77}$	0.50	12/11
2058	...	...	$10.74^{+3.9}_{-2.1}$	$1.82^{+0.75}_{-0.49}$	$0.72^{+0.94}_{-0.77}$	1.64	36/38
0154350101	...	...	$10.73^{+3.8}_{-2.2}$	$1.41^{+0.57}_{-0.40}$	$0.52^{+0.94}_{-0.29}$	1.17	27/26
14801	...	$0.61^{+0.15}_{-0.19}$ (c)	$5.61^{+3.0}_{-3.3}$	$4.02^{+1.5}_{-1.2}$	$0.03^{+0.03}_{-0.02}$	3.24	12/11
16000	...	...	$9.76^{+2.8}_{-1.7}$	$3.19^{+1.2}_{-0.78}$	$0.04^{+0.07}_{-0.02}$	3.70	59/55
16001	...	...	$7.80^{+5.6}_{-3.5}$	$3.85^{+1.6}_{-1.2}$	$0.04^{+0.05}_{-0.02}$	3.90	18/20
16484	...	...	$7.90^{+4.2}_{-2.7}$	$3.68^{+1.6}_{-1.1}$	$0.04^{+0.06}_{-0.02}$	3.80	20/21
16485	...	...	$9.25^{+11}_{-4.5}$	$3.22^{+1.3}_{-1.1}$	$0.04^{+0.08}_{-0.02}$	3.63	13/10
16002	...	...	$6.63^{+1.3}_{-1.6}$	$3.60^{+1.2}_{-0.9}$	$0.03^{+0.04}_{-0.01}$	3.22	51/48
16003	...	...	$>9.5$	$1.40^{+0.83}_{-0.51}$	$0.04^{+0.07}_{-0.02}$	2.34	29/34
0864270101	...	...	$10.46^{+44}_{-3.1}$	$1.04^{+0.98}_{-0.55}$	$0.04^{+0.07}_{-0.02}$	1.84	108/101

**Note.** Simultaneous fitting gives  $\chi^2/\text{dof} = 383/373$ . (a) :  $nH$  fixed to the galactic value. (b) and (c): Linked input photon temperature  $T_0$  and inner disk temperature  $T_{\text{in}}$  for observation with flaring state (Group A) and nonflaring state (Group B and Group C).

calculated for energy range (0.3–10 keV). We find that the hardness ratio is lower in the flaring state compared to the nonflaring state, indicating a higher fraction of soft X-ray flux during flares. We see a trend of increasing hardness with luminosity, which can be explained if the system is being viewed at low inclination. With the increase in accretion rate, the wind opening angle decreases, which causes more hard photons to be geometrically beamed into our line of sight (M. J. Middleton et al. 2015a). However, the presence of a 1 keV feature in low-flux observations suggests that the system might instead be viewed at a moderate inclination, where the wind intersects our line of sight and causes overall flux absorption. Therefore, within the limitation of current data, it is hard to obtain a clear geometrical picture of the source because the two results point to different scenarios.

### 3.2.2. *diskpbb*

Due to the curved spectral shape observed in the nonflaring state, the *diskpbb* model also provides a good fit to the data. It is a multitemperature disk blackbody where temperature varies as a function of  $r$ , where  $r$  is the radial distance along the accretion disk as  $T \propto r^{-p}$  (J. Fukue 1994). For  $p = 0.75$ , it is a standard thin accretion disk (N. I. Shakura & R. A. Sunyaev 1973) accreting at sub-Eddington rate; for  $p < 0.75$ , the disk is affected by advection; and for  $p = 0.5$ , it is referred to as the slim disk (M. Abramowicz et al. 1988), signifying the presence of super-Eddington accretion in the system. Fitting the spectra of the flaring state with *diskpbb* gives unphysically high inner disk temperatures  $T_{\text{in}} > 5$  keV. For the spectra of nonflaring state, we did the analysis of Group B and Group C separately and linked the inner disk temperatures within each group separately. This provides a sufficiently good fit to the data, with  $p$ -values within error bars within each group. We further link the  $p$ -values in these groups, which changes the statistics from  $\chi^2/\text{dof} = 315/306$  to  $\chi^2/\text{dof} = 321/312$ , which is not statistically different. Inner disk temperature for Group B comes out to be  $T_{\text{in}} = 2.07^{+0.55}_{-0.31}$  keV with  $p = 0.60^{+0.04}_{-0.02}$ , whereas for the Group C it is  $T_{\text{in}} = 3.5^{+1.5}_{-1.5}$  keV with  $p < 0.53$ . The  $p$ -values in both groups are lower than  $p = 0.75$  of the standard thin accretion disk, suggesting the advection-dominated flow in the system. Although Group C has a higher best-fit value of  $T_{\text{in}}$  than Group B, these values are within the error bars. We confirmed

this by linking the temperature of the two groups together. This gives us  $\chi^2/\text{dof} = 324/313$  with a common temperature of  $T_{\text{in}} = 2.12^{+0.64}_{-0.32}$  keV for both groups. For a common temperature, Group B has a higher  $p$ -value of  $p = 0.61^{+0.04}_{-0.03}$  with a high flux value as compared to Group C with  $p = 0.52^{+0.04}_{-0.02}$  and a low flux value.

### 3.2.3. *diskbb+diskbb*

Because of the curved spectral shape of the observations in the nonflaring state and their nonvariability below 1 keV, we also fit the spectra with a dual thermal model *diskbb+diskbb*. Here, we link the inner disk temperature  $T_{\text{in}}$  of the cool *diskbb* component among the observations, which takes into account the spectral invariability below 1 keV, keeping the hot *diskbb* component to vary, which is useful in producing the spectral curvature in the spectra. The hot *diskbb* represents the emission from the inner regions of the disk or corona, and cool *diskbb* represents the emission from the outer disk or the massive optically thick outflows. The motivation for using this model for observations in the nonflaring state further comes from the fact that the best XMM observation (Obs. ID—0864270101) with the highest counting statistics provides a good fit for this model with all the parameters well constrained.

Fitting the spectra of the flaring state with this model gives very high hot temperature  $T_{\text{in}}(\text{hot}) \sim 5.0$  keV, and very low normalization values  $\sim (10^{-6} - 10^{-4})$ . Fitting the nonflaring spectra with this model, we link the  $nH$  and the cool temperature  $T_{\text{in}}(\text{cool})$  of all observations as the nonflaring spectra overlap below 1 keV and separately link the hot temperature within Groups B and C. This provides an acceptable fit to the data with  $\chi^2/\text{dof} = 310/305$ . We obtain a cool temperature of  $T_{\text{in}}(\text{cool}) = 0.41^{+0.11}_{-0.08}$  keV and a hot temperature of  $T_{\text{in}}(\text{hot}) = 1.64^{+0.18}_{-0.14}$  keV for Group B and  $T_{\text{in}}(\text{hot}) = 1.88^{+0.65}_{-0.33}$  keV for Group C, respectively. Most of these  $T_{\text{in}}(\text{hot})$  values are consistent within error bars, so we further link the  $T_{\text{in}}(\text{hot})$  between Groups B and C. This does not change the statistics and gives a common cool temperature  $T_{\text{in}}(\text{cool}) = 0.38^{+0.08}_{-0.06}$  keV, hot temperature  $T_{\text{in}}(\text{hot}) = 1.67^{+0.18}_{-0.13}$  keV along with  $nH = 0.12^{+0.05}_{-0.04}$  ( $10^{22} \text{ cm}^{-2}$ ) for both Group B and C, with  $\chi^2/\text{dof} = 311/306$ . Plotting the



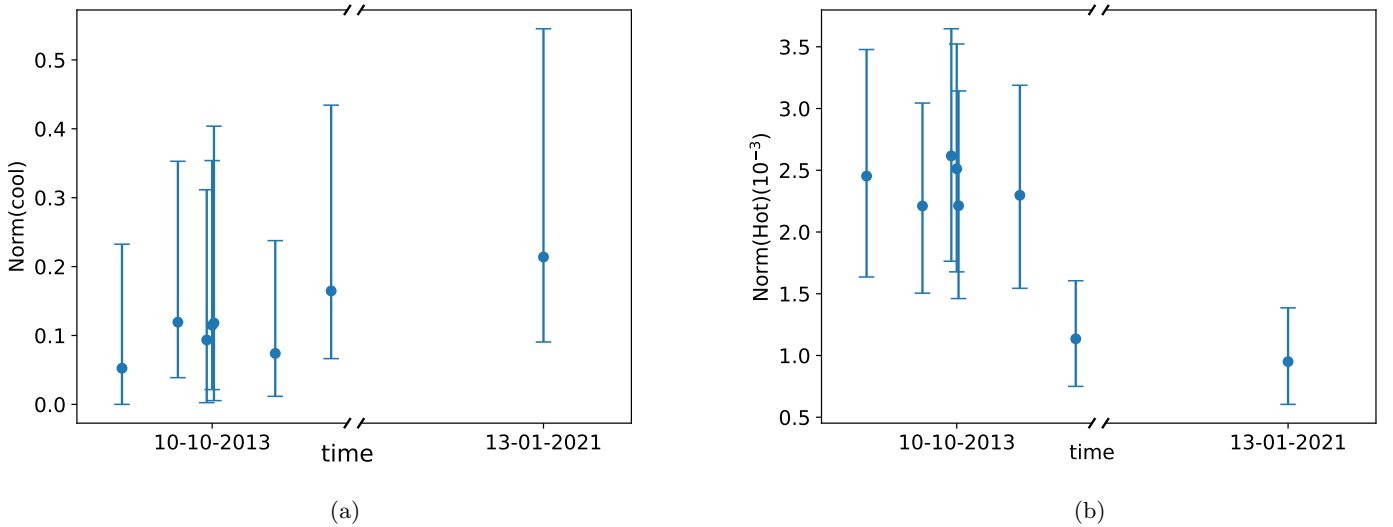


**Figure 5.** Variation of normalization of cool diskbb (Norm(cool)) (a) and hot diskbb component (Norm(hot)) (b) for observations in the nonflaring state using model `tbabs*(diskbb+diskbb)` with linked  $nH$ ,  $T_{in}(\text{cool})$  and  $T_{in}(\text{hot})$ .

normalizations of cool temperature component (Norm(cool)), we see the values are consistent within error bars (Figure 5(a)), which explains the nonvariability in the spectra in the soft X-ray part (below 1 keV). Plotting the normalizations of hot temperature component (Norm(hot)), we see that the values are within error bars for Group B (first six points of Figure 5(b)) as well as for Group C (last two points of Figure 5(b)) separately. This indicates that the spectral shapes and flux values within Groups B and C are similar, with Group B having higher flux values than Group C.

#### 3.2.4. Significance of the 1 keV Feature in the Spectra of Flaring and Nonflaring States

We detect a 1 keV Gaussian feature in the spectra of the flaring state observations. However, this feature is not significant during the observations of the nonflaring state. To compare the significance of this feature between flaring and nonflaring states, we employ `simfittest` in the `xspec`, which generates simulated data sets and uses these data sets to calculate the F-test probability for adding a model component. We use this test to estimate the significance of the Gaussian component in the model `tbabs*(po+gauss)` for both flaring and nonflaring states. We choose the `powerlaw` model as the continuum because it provides sufficiently good statistics for both flaring and nonflaring states with constrained parameters. We fit this model separately for flaring and nonflaring states, linking the line energy  $E_l$  and line width  $\sigma$  between the observations. For flaring spectra, we get line energy of  $E_l \sim 0.96$  keV with line width of  $\sim 0.1$  keV, which is similar to the values generally observed in the ULX sources (M. J. Middleton et al. 2015b; H. M. Earnshaw & T. P. Roberts 2017; H. P. Earnshaw et al. 2019; F. Pintore et al. 2021; T. Ghosh et al. 2022; T. Ghosh & V. Rana 2023). The addition of the Gaussian component improves the statistics from  $\chi^2/\text{dof} = 88/77$  to  $\chi^2/\text{dof} = 68/73$  in the flaring state, which is an improvement of  $\Delta\chi^2 = 20$  for 4 dof. For the nonflaring state, the line energy and line width are not constrained for most of the observations, so we freeze the line energy  $E_l = 0.96$  keV and line width  $\sigma = 0.1$  keV and see the normalization values of the Gaussian component in these observations. We see that only observations with Obs. IDs—

16000, 16001, 16484, 16485, and 16003 have normalization values that are not zero. We further do the simultaneous fitting of these observations where we link the  $E_l$  and  $\sigma$  between them. This changes the statistics from  $\chi^2/\text{dof} = 142/145$  to  $\chi^2/\text{dof} = 135/139$ , which is not statistically different.

We do the `simfittest` for both the analysis (for flaring and nonflaring states) for 10,000 iterations, and we got 99.84% confidence interval, which is a  $\sim 3\sigma$  significance result for the flaring state. For a nonflaring state, this comes out to be 78.3%, which is a  $\sim 1.2\sigma$  result. This strongly suggests the prominent presence of a 1 keV line feature in the flaring state, as compared to the nonflaring state.

## 4. Discussion

### 4.1. Spectral Difference between Flaring and Nonflaring States

We analyze 11 XMM-Newton and Chandra observations of M74 X-1 between 2001 and 2021 and study its long-term spectral and timing properties. Initial observations (Obs. IDs: 2057, 2058, and 0154350101) were studied by J.-F. Liu et al. 2005 and M. Krauss et al. 2005, which revealed flaring behavior in the source. For completeness, we reanalyze these observations in the flaring state and more recent observations of the source that did not show any flaring events. The flaring states with lower average flux show two-component-like spectra, which include a soft thermal component and a hard power-law component. In contrast, nonflaring states have higher flux and curved single-component spectra. Comparing the general spectral variability of ULX sources with M74 X-1, we see that similar spectral evolution has also been observed in other ULX sources, such as NGC 1313 X-1 (G. C. Dewangan et al. 2010), NGC 1313 X-2 (A. Robba et al. 2021), and Ho IX X-1 (W. Luangtip et al. 2016; V. Jithesh et al. 2017; D. Walton et al. 2017).

For the flaring state, we identify the best-fit model as `tbabs*(diskbb+po)` with  $\Gamma = 1.3^{+0.30}_{-0.35}$  and  $T_{in} = 0.28^{+0.04}_{-0.04}$  keV. We also detect a 1 keV line feature with  $E_{line} = 0.96^{+0.05}_{-0.11}$  keV and  $\sigma = 0.11^{+0.13}_{-0.06}$  keV in the spectra of the flaring state, which is not significant in the nonflaring state. Such emission feature has been reported in several other ULX sources such as

NGC 6946 X-1, NGC 4395 X-1, NGC 1313 X-1, NGC 5408 X-1, NGC 55 X-1, Ho IX X-1, and Ho II X-1 (M. J. Middleton et al. 2015b; C. Pinto et al. 2016, 2017; T. Ghosh et al. 2022; T. Ghosh & V. Rana 2023). These residues suggest the presence of outflows in the system, which further implies the presence of super-Eddington accretion in the system.

From the hardness–luminosity diagram, we see that flaring states (showing the 1 keV feature) have a higher fraction of soft X-ray flux than nonflaring states. This has been reported for several ULX sources where the 1 keV feature was most prominent in the softer spectra (P. Kosec et al. 2021). The variation of 1 keV feature from soft (flaring) to hard (nonflaring) spectra can be explained using the wind model in super-Eddington accretion (J. Poutanen et al. 2007; M. J. Middleton et al. 2015b). If our line of sight passes through the wind, we observe emission and absorption features in the spectra that are formed by the interactions of hard photons with the wind. We also receive a high fraction of the soft X-ray flux due to the downscattering of hard photons from the wind. Therefore, the presence of the 1 keV Gaussian feature and a higher fraction of soft X-ray flux in the observations with flaring state suggest that the wind is in our line of sight during the flaring state, whereas it is out of our line of sight during nonflaring states. The presence of wind features in low-flux observations suggests that the system is being viewed at moderate inclinations where the wind is crossing our line of sight. However, the observed increase in hardness with luminosity suggests that the system is being viewed at a low inclination where the central regions of the accretion disk are not completely obscured by the outflowing wind. At low inclination, an increase in the accretion rate causes the wind funnel to narrow, leading to more hard photons being geometrically beamed into our line of sight (A. King 2009). This results in the observed trend of an increase in hardness with luminosity. Similar behavior was observed in Ultraluminous X-ray Pulsar (ULXP) NGC 1313 X-2, where traces of wind were found in low-flux observations and there is a trend of increasing hardness with luminosity (M. J. Middleton et al. 2015a). Recently, a harder when brighter effect along with the 1 keV residue feature in the spectra was also observed in one potential ULX pulsar candidate, NGC 4559 X-7 (F. Pintore et al. 2025). To further investigate the presence of the wind feature during the flaring state at low and high count rates, we divide the spectrum of Obs ID: 2058 in the flaring state based on the count rate. We select Obs ID: 2058 for this analysis since flaring is the most prominent and regular in this observation, and also has sufficient statistics for such an analysis. We extract the spectrum with a count rate  $>0.03 \text{ count s}^{-1}$  and call it the bright spectrum. Similarly, we extract the spectrum with a count rate  $<0.03 \text{ count s}^{-1}$  and call it the faint spectrum. We model both spectra with a power-law continuum and add a Gaussian component to account for the 1 keV residue due to the wind. We do the `simfittest` on the Gaussian component for 10,000 iterations to check the significance of this Gaussian component. We find a 99.7% confidence interval for the faint spectrum, which is a  $3\sigma$  significance result, whereas, for the bright spectrum, we get an 85.8% confidence interval, which is equivalent to the  $1.44\sigma$  result. This shows the wind feature to be more prominent in the faint spectra as compared to the bright spectra. This can occur if the wind crosses our line of sight, resulting in significant photon absorption and causing a

low flux state with enhanced wind features. We tried a similar analysis with other observations in the flaring state, but the statistics were not sufficient for such a division of spectra. A 1 keV wind feature along with a QPO has also recently been observed in one observation of the ULXP M51 ULX-7 (M. Imbrogno et al. 2024), where a similar super-Eddington accreting wind model was used to explain the QPO. Here, the puffed-up accretion disk, formed due to super-Eddington accretion, generates an outflowing wind with quasi-periodic recurrence, resulting in quasi-periodic variations in the light curve. We have discussed more about the presence of wind and its association with QPO in Section 4.3.

#### 4.2. Mass and Inner Radius Estimates of the Compact Object and Accretion Disk

Using `diskbb+diskbb` model, we get cool temperature of  $T_{\text{in}}(\text{cool}) = 0.38^{+0.08}_{-0.06} \text{ keV}$  whereas the hot temperature is  $T_{\text{in}}(\text{hot}) = 1.67^{+0.18}_{-0.13} \text{ keV}$  for observations in nonflaring state. Plotting the normalizations of the two `diskbb` components (Figure 5), we see that  $\text{Norm}(\text{cool})$  stays within the error bars (Figure 5(a)), signifying no variability below  $\sim 1 \text{ keV}$ . The normalization of hot `diskbb`  $\text{Norm}(\text{hot})$  (Figure 5(b)) is within error bars for Groups B and C separately, with Group B having most of the values higher than that of Group C. We calculate the inner radius of the accretion disk from the normalization factor of hot `diskbb` component using the formula  $R_{\text{in}} = \xi \kappa^2 \sqrt{(\text{Norm} * D_{10}^2) / \cos(i)}$ , where  $D_{10}$  is the distance to the source in units of 10 kpc,  $i$  is the angle of inclination of the disk with our line of sight,  $\xi$  is the geometric factor, and  $\kappa$  is the color correction factor (A. Kubota et al. 1998). For `diskbb`, we take  $\xi = 0.412$  and  $\kappa = 1.7$  (A. Kubota et al. 1998). Since the  $\text{Norm}(\text{hot})$  is different for Groups B and C, we calculate hot `diskbb` inner radii for both groups separately. We get  $R_{\text{in},B}(\text{hot}) = 54^{+10}_{-10} (\cos i)^{-1/2} \text{ km}$  and  $R_{\text{in},C}(\text{hot}) = 36^{+7}_{-7} (\cos i)^{-1/2} \text{ km}$ , respectively. Assuming a moderate inclination angle of  $i \sim 60^\circ$ , inner radius comes out to be  $R_{\text{in},B}(\text{hot}) = 77^{+14}_{-14} \text{ km}$  and  $R_{\text{in},C}(\text{hot}) = 50^{+11}_{-9} \text{ km}$ . To calculate the compact object’s mass from the inner radius of the accretion disk, we use the average radius  $R_{\text{in,avg}}(\text{hot})$  of Groups B and C, which comes out to be  $R_{\text{in,avg}}(\text{hot}) = 64^{+13}_{-12} \text{ km}$ . Assuming that for the black hole compact object, the inner radius of the accretion disk touches the inner stable circular orbit (ISCO), we get the mass of the compact object as  $M = 7.1^{+1.4}_{-1.3} M_{\odot}$ . This comes under the stellar-mass black hole (sMBH) regime and signifies super-Eddington accretion in the system. Using the steps highlighted in Section 4.4 of T. Ghosh & V. Rana 2023, we calculate the mass accretion rate in the units of the Eddington accretion rate, i.e.,  $\dot{m}_0 = \dot{M}_0 / \dot{M}_{\text{Edd}}$  and the spherization radius  $R_{\text{sph}}$  for both Groups B and C. Taking the mean luminosity from each group,  $L_B = 3.48 \times 10^{39} \text{ erg s}^{-1}$  and  $L_C = 1.94 \times 10^{39} \text{ erg s}^{-1}$ , and taking  $m_1 = 7.1$ , we obtain  $\dot{m}_0 \approx 9$  and  $\dot{m}_0 \approx 7$  for Groups B and C, respectively. The spherization radius comes out to be  $R_{\text{sph},B} = 1296^{+264}_{-243} \text{ km}$  and  $R_{\text{sph},C} = 1008^{+205}_{-189} \text{ km}$ . The inner radius of the hot `diskbb` component is smaller than the spherization radius of both groups  $R_{\text{in}(B,C)}(\text{hot}) < R_{\text{sph}(B,C)}$ , indicating that this component is likely reproducing the super-Eddington inner accretion flow within the spherization radius  $R_{\text{sph}}$ .

### 4.3. Quasi-periodic Modulation, Its Explanation and Association with Wind

We detect a 1 keV wind feature in the spectra of the observations in the flaring state. These same observations have previously been reported to exhibit quasi-periodicities by M. Krauss et al. (2005) and J.-F. Liu et al. (2005). This is similar to the heartbeat oscillations shown by 4XMM J111816.0-324910 (S. Motta et al. 2020) and quasi-periodic modulations shown by 4XMM J140314.2+541806 (R. T. Urquhart et al. 2022). Similar modulation with the traces of wind in the same observation has also been recently reported in a ULXP M51 ULX-7 (M. Imbrogno et al. 2024). All these sources have similar timescales of modulation, giving rise to the mHz QPOs. Previous studies have proposed various models to explain these modulations, such as the limit cycle instability driven by the Lightman–Eardley radiation pressure instability for 4XMM J111816.0-324910 and Lense–Thirring precession of an outflow from the inner regions of the disk (M. Middleton et al. 2019) for 4XMM J140314.2+541806 and M51 ULX-7. To understand the quasi-periodic modulation in M74 X-1, we divide the spectrum of the observation with flaring state, Obs Id: 2058, (showing highest modulation in the light curve), on the basis of the count rate: bright spectra (count rate > 0.03 counts/s) and faint spectra (count rate < 0.03 counts/s) and fit it with the model `diskbb+diskbb` to see the evolution of spectral parameters of the hard and soft spectral components with the count rate. We found that the spectral parameters do not change with the count rate, which is in contrast with the source 4XMM J111816.0-324910, where a clear evolution in the spectral parameters has been observed in the different phases of the modulation. In addition, modulation in 4XMM J111816.0-324910 is more regular and stable, similar to the  $\rho$  class variability found in GRS 1915+105 (T. Belloni et al. 2000), whereas the variability in M74 X-1 is quite irregular. All these observations suggest that modulation in M74 X-1 is different from that in 4XMM J111816.0-324910, and thus limit cycle instability may not be the possible explanation for M74 X-1 QPO. Compared to other sources, the modulation properties of M74 X-1 closely resemble those of M51 ULX-7, where similar irregularity in the flares with no change in the spectral parameters with count rate has been observed (M. Imbrogno et al. 2024). Another similarity between M74 X-1 and M51 ULX-7 is the presence of a 1 keV wind feature in the same observations where a QPO is reported, which suggests that Lense–Thirring precession (used to explain QPOs in M51 ULX-7) could be responsible for the quasi-periodicity in M74 X-1 as well. Moreover, the occurrence of QPOs in certain observations and their absence in others further suggests the potential presence of precession in the system. As M. Middleton et al. (2019) pointed out, the strength of the QPO feature is influenced by the inclination angle of the precessing system. If the inclination angle is small (with a small precessing cone), QPO features tend to be weak because the outflowing wind does not obscure our line of sight. However, as the inclination angle increases, the QPO features become more pronounced. This occurs because the line of sight alternates between pointing directly at the central accretion disk and passing through the wind, leading to modulation in the light curve. This might explain why QPO features are present in only a few observations while being absent in other observations. However, unlike M51 ULX-7, which exhibits a  $\sim 39$  days

super-orbital periodicity (G. Vasilopoulos et al. 2020), attributed to the precessing wind period ( $P_{\text{wind}}$ ) in the context of Lense–Thirring precession (M. Middleton et al. 2019), no such periodicity has been reported for M74 X-1. Therefore, this explanation remains unconfirmed and further requires long-term monitoring of the source to confirm this.




## 5. Conclusions

In this paper, we report the long-term spectral and timing evolution of ULX source M74 X-1 using 11 archival XMM-Newton and Chandra observations. We see that some observations show flaring activity in them, whereas in others it is absent. Observations in the flaring state have two-component spectra with low flux values, whereas the nonflaring state has single-component spectra with high flux values. This spectral evolution is very similar to the spectral evolution of NGC 1313 X-1 (G. C. Dewangan et al. 2010), NGC 1313 X-2 (A. Robba et al. 2021), and Ho IX X-1 (W. Luangtip et al. 2016; D. Walton et al. 2017; V. Jithesh et al. 2017). Spectra of both flaring and nonflaring states are well described by models such as `powerlaw`, `diskbb+powerlaw`, and the Comptonizing corona model `diskbb+comptt` with low plasma temperature and high optical depth. Because of the curved spectral shape of observations in the nonflaring state, they are also well described by other models such as `cutoffpl`, `diskbb+diskbb`, `diskpbb`. The flaring state has softer spectra compared to the nonflaring state and displays a 1 keV Gaussian feature in the spectra, which is not significant in the nonflaring state. This feature has been reported in several ULX sources and is more prominent in the softer spectra, aligning with current findings. This feature could indicate the presence of powerful outflows, which further indicates the presence of super-Eddington accretion in the system. QPOs were reported for this source by M. Krauss et al. (2005) and H. Avdan & S. Avdan (2024), which can be explained by the presence of wind in our line of sight with quasi-periodic occurrence or the Lense–Thirring precession of an outflow from an inner region of the disk, similar to the ULXP M51 ULX-7. M. Krauss et al. (2005) suggested that M74 X-1 is an IMBH on the basis of low accretion disk temperature. In our analysis, we estimate the mass of the compact object from the hot `diskbb` component in `diskbb+diskbb`, assuming that the inner accretion disk radius truncates at the ISCO, which comes out to be  $M = 7.1^{+1.4}_{-1.3} M_{\odot}$ . This comes under the sMBH regime, with super-Eddington accretion happening in the system. Furthermore, the similarities between the M74 X-1 and the known ULXP, such that NGC 1313 X-2 and M51 ULX-7, suggest that it could also be a potential neutron star candidate.

## Data Availability

This paper utilizes XMM-Newton and Chandra archival data available at the High Energy Astrophysics Science Archive Research Center (HEASARC) (accessible at <https://heasarc.gsfc.nasa.gov/cgi-bin/W3Browse/w3browse.pl>). The Chandra data sets are obtained by the Chandra X-ray Observatory, contained in DOI: 10.25574/cdc.347.

## ORCID iDs

Aman Upadhyay  <https://orcid.org/0009-0000-2039-4340>  
 Tanuman Ghosh  <https://orcid.org/0000-0002-3033-5843>  
 Vikram Rana  <https://orcid.org/0000-0003-1703-8796>

## References

- Abramowicz, M., Czerny, B., Lasota, J., et al. 1988, *ApJ*, **332**, 646
- Arnaud, K. 1996, in ASP Conf. Ser. 101, *Astronomical Data Analysis Software and Systems V*, ed. H. J. George & B. Jeannette (San Francisco, CA: ASP), 17
- Avdan, H., & Avdan, S. 2024, *A&A*, **690**, A335
- Avdan, S., Akyuz, A., Acar, S., et al. 2023, *MNRAS*, **519**, 4826
- Bachetti, M., 2018 *Astrophysics Source Code Library*, ascl:1805.019
- Bachetti, M., Harrison, F., Walton, D. J., et al. 2014, *Natur*, **514**, 202
- Belloni, T., Klein-Wolt, M., Méndez, M., Van Der Klis, M., & Van Paradijs, J. 2000, *A&A*, **355**, 271
- Brightman, M., Harrison, F. A., Fürst, F., et al. 2018, *NatAs*, **2**, 312
- Carpano, S., Haberl, F., Maitra, C., & Vasilopoulos, G. 2018, *MNRAS: Letters*, **476**, L45
- Castillo, G. R., Israel, G. L., Belfiore, A., et al. 2020, *ApJ*, **895**, 60
- Colbert, E. J., & Mushotzky, R. F. 1999, *ApJ*, **519**, 89
- Dewangan, G. C., Misra, R., Rao, A., & Griffiths, R. 2010, *MNRAS*, **407**, 291
- Earnshaw, H. P., Grefenstette, B. W., Brightman, M., et al. 2019, *ApJ*, **881**, 38
- Earnshaw, H. M., & Roberts, T. P. 2017, *MNRAS*, **467**, 2690
- Earnshaw, H. M., Roberts, T. P., Heil, L. M., et al. 2016, *MNRAS*, **456**, 3840
- Feng, H., Tao, L., Kaaret, P., & Grisé, F. 2016, *ApJ*, **831**, 117
- Fukue, J. 1994, *ApJ*, **426**, 308
- Fürst, F., Walton, D., Harrison, F., et al. 2016, *ApJL*, **831**, L14
- Ghosh, T., & Rana, V. 2023, *ApJ*, **949**, 78
- Ghosh, T., Rana, V., & Bachetti, M. 2022, *ApJ*, **938**, 76
- Gladstone, J. C., Roberts, T. P., & Done, C. 2009, *MNRAS*, **397**, 1836
- Imbrogno, M., Motta, S. E., Amato, R., et al. 2024, *A&A*, **689**, A284
- Israel, G. L., Belfiore, A., Stella, L., et al. 2017a, *Sci*, **355**, 817
- Israel, G. L., Papitto, A., Esposito, P., et al. 2017b, *MNRAS: Letters*, **466**, L48
- Jithesh, V., Misra, R., & Wang, Z. 2017, *ApJ*, **849**, 121
- Kaaret, P., Feng, H., & Roberts, T. P. 2017, *ARA&A*, **55**, 303
- Kajava, J. J. E., & Poutanen, J. 2009, *MNRAS*, **398**, 1450
- King, A. 2009, *MNRAS: Letters*, **393**, L41
- Kong, A., & Di Stefano, R. 2003, *ApJ*, **590**, L13
- King, A., Lasota, J.-P., & Middleton, M. 2023, *NewAR*, **96**, 101672
- Kosec, P., Pinto, C., Reynolds, C., et al. 2021, *MNRAS*, **508**, 3569
- Krauss, M., Kilgard, R., Garcia, M., Roberts, T., & Prestwich, A. 2005, *ApJ*, **630**, 228
- Kubota, A., Tanaka, Y., Makishima, K., et al. 1998, *PASJ*, **50**, 667
- Liu, J.-F., Bregman, J. N., Lloyd-Davies, E., et al. 2005, *ApJ*, **621**, L17
- Luangtip, W., Roberts, T. P., & Done, C. 2016, *MNRAS*, **460**, 4417
- Middleton, M., Fragile, P., Ingram, A., & Roberts, T. 2019, *MNRAS*, **489**, 282
- Middleton, M. J., Heil, L., Pintore, F., Walton, D. J., & Roberts, T. P. 2015a, *MNRAS*, **447**, 3243
- Middleton, M. J., Walton, D. J., Fabian, A., et al. 2015b, *MNRAS*, **454**, 3134
- Miller, J. M., Fabian, A., & Miller, M. 2004, *ApJ*, **614**, L117
- Motta, S., Marelli, M., Pintore, F., et al. 2020, *ApJ*, **898**, 174
- Pinto, C., Alston, W., Soria, R., et al. 2017, *MNRAS*, **468**, 2865
- Pinto, C., Middleton, M. J., & Fabian, A. C. 2016, *Natur*, **533**, 64
- Pintore, F., Marelli, M., Salvaterra, R., et al. 2020, *ApJ*, **890**, 166
- Pintore, F., Motta, S., Pinto, C., et al. 2021, *MNRAS*, **504**, 551
- Pintore, F., Pinto, C., Rodriguez-Castillo, G., et al. 2025, *A&A*, **695**, A238
- Pintore, F., Zampieri, L., Wolter, A., & Belloni, T. 2014, *MNRAS*, **439**, 3461
- Poutanen, J., Lipunova, G., Fabrika, S., Butkevich, A. G., & Abolmasov, P. 2007, *MNRAS*, **377**, 1187
- Robba, A., Pinto, C., Walton, D. J., et al. 2021, *A&A*, **652**, A118
- Roberts, T. P. 2007, *Ap&SS*, **311**, 203
- Sathyaprakash, R., Roberts, T., Walton, D., et al. 2019, *MNRAS*, **488**, L35
- Shakura, N. I., & Sunyaev, R. A. 1973, *A&A*, **24**, 337
- Soria, R., & Kong, A. K. 2002, *ApJ*, **572**, L33
- Stobart, A.-M., Roberts, T., & Wilms, J. 2006, *MNRAS*, **368**, 397
- Sutton, A. D., Roberts, T. P., & Middleton, M. J. 2013, *MNRAS*, **435**, 1758
- Tsygankov, S., Doroshenko, V., Lutovinov, A., Mushtukov, A., & Poutanen, J. 2017, *A&A*, **605**, A39
- Urquhart, R. T., Soria, R., Di Stefano, R., et al. 2022, *MNRAS*, **511**, 4528
- Vasilopoulos, G., Lander, S., Koliopoulos, F., & Bailyn, C. 2020, *MNRAS*, **491**, 4949
- Verner, D., Ferland, G. J., Korista, K., & Yakovlev, D. 1996, *ApJ*, **46**, 487
- Walton, D., Fürst, F., Harrison, F., et al. 2017, *ApJ*, **839**, 105
- Walton, D., Fürst, F., Heida, M., et al. 2018, *ApJ*, **856**, 128
- Walton, D., Middleton, M., Rana, V., et al. 2015, *ApJ*, **806**, 65
- Walton, D., Pinto, C., Nowak, M., et al. 2020, *MNRAS*, **494**, 6012
- Walton, D. J., Harrison, F., Grefenstette, B., et al. 2014, *ApJ*, **793**, 21
- Walton, D. J., Mackenzie, A., Gully, H., et al. 2022, *MNRAS*, **509**, 1587
- Wilms, J., Allen, A., & McCray, R. 2000, *ApJ*, **542**, 914
- Wilson-Hodge, C. A., Malacaria, C., Jenke, P. A., et al. 2018, *ApJ*, **863**, 9